RAA 2019 Vol. **19** No. **6**, 81(12pp) doi: 10.1088/1674–4527/19/6/81

http://www.raa-journal.org *http://iopscience.iop.org/raa*

Research in Astronomy and Astrophysics

The morphology, kinematics and metallicity of blue-core galaxies

Yong-Yun Chen, Yan-Mei Chen*, Qiu-Sheng Gu, Yong Shi, Long-Ji Bing and Xiao-Ling Yu

School of Astronomy and Space Science, Nanjing University, Nanjing 210093, China; *chenym@nju.edu.cn*
Collaborative Innovation Center of Modern Astronomy and Space Exploration, Nanjing 210093, China

Received 2018 June 30; accepted 2018 December 5

Abstract We select 107 blue-core galaxies from the MaNGA survey, studying their morphology, kinematics as well as the gas-phase metallicity. Our results are as follows: (i) In our sample, 26% of blue-core galaxies have decoupled gas-star kinematics, indicating external gas accretion; 15% have bar-like structure and 8% show post-merger features, such as tidal tails and irregular gas/star velocity field. All these processes/features, such as accreting external misaligned gas, interaction and bar, can trigger gas inflow. Thus the central star-forming activities lead to bluer colors in their centers (blue-core galaxies). (ii) By comparing with the SDSS DR7 star-forming galaxy sample, we find that the blue-core galaxies have higher central gas-phase metallicity than what is predicted by the local mass-metallicity relation. We explore the origin of the higher metallicity, finding that not only the blue-core galaxies, but also the flat-gradient and red-core galaxies all have higher metallicity. This can be explained by the combined effect of redshift and galaxy color.

Key words: galaxies: abundances — galaxies: formation — galaxies: structure

1 INTRODUCTION

Many of the properties of galaxies (including the galaxy color-magnitude diagram) indicate that there are fundamentally two types of galaxies. These groups are divided into blue star-forming galaxies that are more like spiral types, and red non-star forming galaxies that are more like elliptical galaxies. The elliptical galaxies have smoothly varying brightness, which steadily decreases outward from the center. They appear elliptical in shape, with lines of equal brightness composed of concentric and similar ellipses. They are also devoid of gas and dust, and only contain old stars. Moreover, the spiral galaxies are conspicuous for their spiral shaped arms, which emanate from or near the nucleus and gradually wind outward to the edge. The arms are embedded in a thin disk of stars. Both the arms and disk of a spiral system are blue in color. Generally speaking, a galaxy is constructed by a central bulge with an old stellar population plus an outskirt disk with young stellar populations. The classification of one galaxy into elliptical or spiral depends on the relative contributions of the bulge and disk. In this galaxy structure picture, we would expect the stellar population ages decrease with increasing radii (indicating mass assembly is finished earlier in the galaxy center than the outskirts, which is known as the "inside-out" scenario) or stay constant (i.e., in pure disk galaxies with no contribution from bulge or pure elliptical galaxies with no disk contribution).

The "outside-in" evolutionary scenario has also been studied in detail individually, such as in the Large Magellanic Cloud (Gallart et al. 2008). Based on multi-wavelength broad-band photometry, Pan et al. (2015) found a group of galaxies with younger stellar populations in the center than the outskirts. This group is inferred to arise from the "outside-in" evolutionary scenario. A full understanding of galaxy evolution mode as well as the cessation of star formation requires spatially resolved observation of stellar and gas components. Integral field unit (IFU) surveys that obtained spatially resolved spectra for samples of galaxies in the last decades have greatly improved our conception of galaxy formation and evolution. Li et al. (2015) classified 12 galaxies observed by P-MaNGA as either centrally quiescent (CQ) or centrally star-forming. They found that CQ galaxies represent negative radial gradients in D_n4000, which supports that CQ

* Corresponding author.

galaxies obey the inside-out assembly mode. Pérez et al. (2013) used integral field spectroscopic data to study the star formation histories (SFH) of 105 galaxies in the local Universe from observations of the Calar Alto Legacy Integral Field Area (CALIFA). They concluded that galaxies with mass more than $M_* \sim 5 \times 10^9\, M_\odot$ grow inside-out, while lower mass galaxies grow outside-in. Wang et al. (2018) studied the radial gradients of low-redshift galaxies observed by the Mapping Nearby Galaxies at Apache Point Observatory (MaNGA) survey. They found that star formation cessation in galaxies depends on stellar mass and structural properties. The evolutionary scenario of galaxies is the "inside-out" assembly mode when stellar mass is more than $\sim 10^{10}\, M_\odot$. Generally speaking, the galaxies following "inside-out" assembly mode have negative color, stellar age and D_n4000 gradients, while the galaxies undergoing "outside-in" assembly mode have positive color, stellar age and D_n4000 gradients (e.g., Wang et al. 2011; Lin et al. 2013).

As the sample size of the surveys increases, more and more galaxies obeying the "outside-in" evolutionary scenario have been found. In this work, we focus on the formation scenario of galaxies with younger stellar populations in the central region (we refer to these as blue-core galaxies), as well as their properties. Section 2 describes the data and sample. In Section 3, we study the morphology and kinematics as well as central gas phase metallicity of these galaxies. In Section 4, we summarize our results. The cosmology parameters $\Omega = 0.3$, $\Lambda = 0.7$ and $H_0 = 100\,\mathrm{km\,s^{-1}}\,h$ Mpc (with $h = 0.7$) are adopted in this work.

2 DATA AND SAMPLE

2.1 The MaNGA Survey

MaNGA is a multi-object IFU survey (Bundy et al. 2015), which is one of three core programs in the fourth phase of the Sloan Digital Sky Survey (SDSS-IV). This utilizes the Baryon Oscillation Spectroscopic Survey (BOSS) spectrograph (Gunn et al. 2006; Smee et al. 2013) to obtain spatially resolved spectroscopy for ∼10 000 nearby galaxies at an effective spatial resolution of $2.5''$. The wavelength coverage of the BOSS spectrographs is from 3600 to 10 300 Å with a spectral resolution $R \sim 2000$ (Drory et al. 2015; Smee et al. 2013). MaNGA has five different types of hexagonal IFUs (Drory et al. 2015): $2\times N_{19}$ ($12''$ in diameter), $4\times N_{37}$, $4\times N_{61}$, $2\times N_{91}$ and $5\times N_{127}$ ($32''$). For a single plate, 17 galaxies are observed simultaneously by using different IFU fiber bundles. A more detailed introduction for the MaNGA survey and instrumentation can be found in Bundy et al. (2015) and Drory et al. (2015), respectively. Law et al. (2015) have also described the MaNGA observing strategy in detail.

MaNGA targets are selected from the SDSS 'Main' galaxy sample (Strauss et al. 2002). The sample is complete at $M_* > 10^9\, M_\odot$ and has a roughly flat $\log M_*$ distribution. The MaNGA sample is composed of three subsamples with different radial coverages (Wake et al. 2017). A primary subsample reaches 1.5 effective radii (R_e in r-band), which accounts for about 5000 galaxies. In addition to the primary subsample, the color-enhanced subsample adds an additional ∼1700 galaxies which is designed to balance the color distribution at a certain M_*. We refer to the primary and color enhanced subsamples as "Primary +." The secondary subsample includes 3300 galaxies with a coverage of 2.5 R_e. The MaNGA sample and data products used here are drawn from the internal MaNGA product Launch-5 (MPL5), which includes ∼ 2721 galaxies observed through July 2015 (the first and second years of the survey). The observed data are reduced by the MaNGA data reduction pipeline (DRP; Law et al. 2015, 2016; Yan et al. 2016).

2.2 Sample Selection

In this work, we use the data analysis pipeline (DAP) products named SPX-GAU-MILESHC (analysis of each individual pixel). To get the radial profile of D_n4000, we use the effective radius R_e, position angle (PA) and ellipticity from the NASA-Sloan Atlas (Abazajian et al. 2009; Blanton et al. 2011), binning the data into different radii, with a bin size of 0.1 R_e.

In Figure 1, the first column shows the SDSS g, r, i images; the second column displays D_n4000 as a function of radius. The black dots represent D_n4000 values for each spaxel with median spectral signal-to-noise ratio (S/N) greater than 5 per pixel and the red dots are the medians. Regarding how to bin the data, the third column gives examples of $0.9\,R_\mathrm{e} - 1.0\,R_\mathrm{e}$ in the form of annuli (white ellipses). These panels depict the D_n4000 map, and the black solid lines delineate the PAs. We then define the radial gradient of D_n4000 in units of dex/R_e as

$$\nabla D_n4000 = dD_n4000/dR\,, \quad (1)$$

where R is the radius in units of effective radius R_e. We use linear regression to fit the median value of D_n4000 (red dots) at $R < R_\mathrm{e}$ for each galaxy, and define the slope as the gradient of D_n4000. The linear regression is performed by using the IDL procedure 'ROBUST_LINEFIT'. Other derived parameters used in this work, such as total star for-

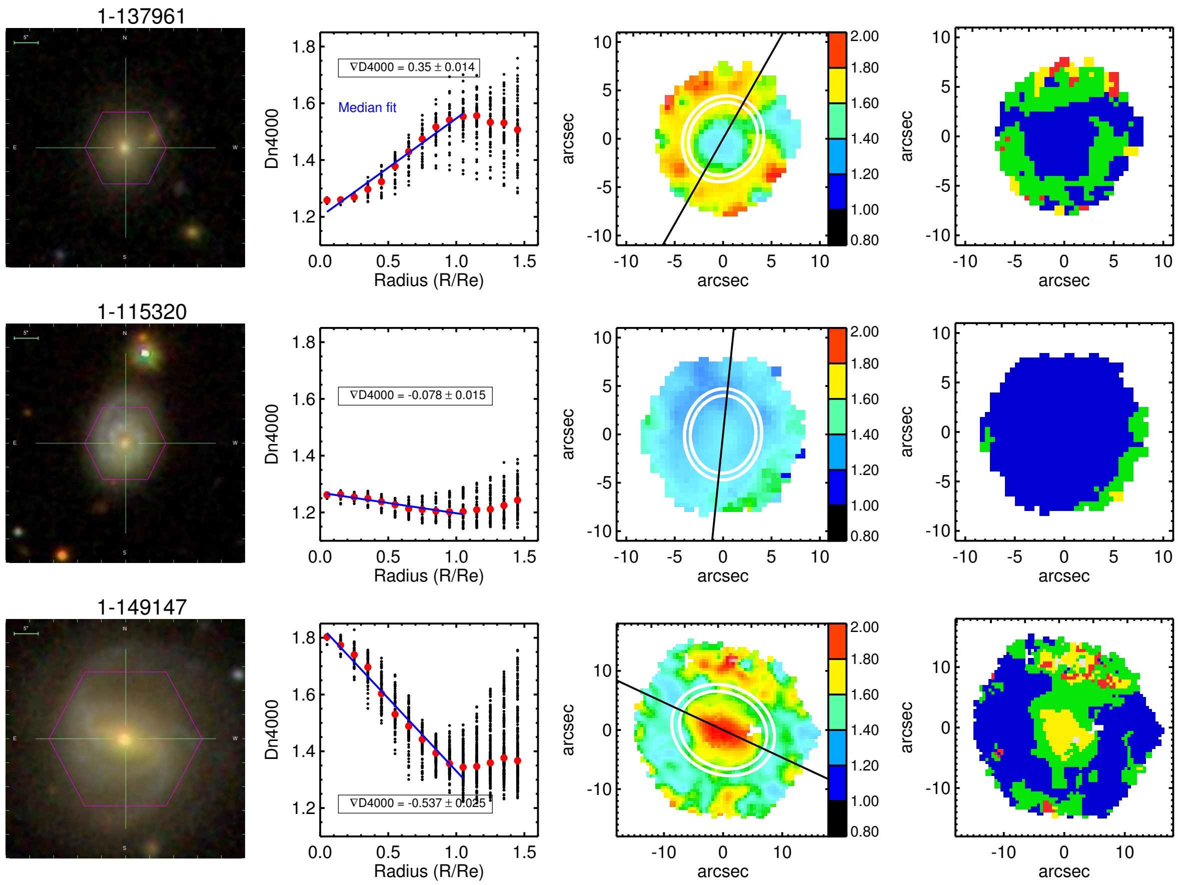

Fig. 1 Examples of galaxies with different $D_n 4000$ gradients. From top to bottom: we show galaxies with positive gradient, flat gradient and negative gradient, respectively. The left column shows the SDSS g, r, i–band images. The second column displays $D_n 4000$ gradients, in which the *black dots* represent values of $D_n 4000$ in bins of 0.1 R_e. The *red dots* are the median values of the *black dots* for each radial bin. The *blue lines* indicate the linear regressions of the *red dots*. The third column features the $D_n 4000$ maps, and the *white ellipses* are 0.9 R_e and 1 R_e. The *black solid lines* mark the PAs. The fourth column depicts the spatially resolved BPT diagram, with the *blue area* representing the star-forming region, *red* means Seyfert, *green* signifies the composite of both AGN and star forming, and *yellow* refers to LIER.

mation rate (SFR) and stellar mass (M_*), are taken from the MPA/JHU catalog [1] (Brinchmann et al. 2004; Tremonti et al. 2004). We match the 2721 MaNGA galaxies with the MPA/JHU catalog, finding 2458 matches. We then select the blue-core galaxy sample according to the following criteria:

(1) $\log \Sigma_{M_*} > 9.7$, where Σ_{M_*} is the stellar mass surface density defined as $\Sigma_{M_*} = 0.5 M_* / \pi R_\mathrm{e}^2$. Through this criterion, we exclude 293 galaxies with low stellar mass surface density. We visually inspect these 293 galaxies by eye, finding that they are dominated by irregular morphology, for which it is hard to derive robust $D_n 4000$ gradients.

(2) We also exclude 60 ongoing merging system by eye since it is hard to define $D_n 4000$ gradient for these systems.

(3) $\nabla D_n 4000 > 0.1$. This criterion ensures that we are selecting galaxies with positive $D_n 4000$ gradient (blue-core galaxies).

We notice that there are some bar galaxies with '∪' or '∩' shaped $D_n 4000$ gradient in these cases, and the associated linear fittings always give a low value of $D_n 4000$ (smaller than 0.1), thus they are not included in our blue-core sample. Finally, there are 107 galaxies in the MPL5 satisfying these selection criteria. In addition to the blue-core galaxies, we also define two other subsamples, one with $\nabla D_n 4000 < -0.1$ and the other with $|\nabla D_n 4000| < 0.1$. We will refer to them as "red-core" and "flat-gradient" galaxies in the following sections, respectively. These three categories are shown in Figure 1 with the blue-core ex-

[1] `http://wwwmpa.mpa-garching.mpg.de/SDSS/DR7/oh.html`

ample in the top row, and the second and third rows providing examples of flat-gradient and red-core galaxies, respectively. The last column in Figure 1 shows the spatially resolved Baldwin, Phillips and Terlevich (BPT) diagram (Baldwin et al. 1981), with the blue area representing the star-forming region, red being Seyfert, green signifying the composite of both active galactic nuclei (AGN) and star forming, and yellow indicating Low-Ionization Emission-Line Region. For the BPT diagram, we use the criterion described in Kewley et al. (2001) and Kauffmann et al. (2003) to separate the AGN, star forming and composite cases as well as the Low-Ionization Emission-Line Regions (LIERs). In summary, there are 969 "flat-gradient" galaxies and 1029 "red-core" galaxies.

3 RESULTS

3.1 Morphology and Kinematics of Blue-core Galaxies

For the blue-core galaxies, strong positive gradients in the 4000 Å break indicate young stellar populations existing in the central regions rather than their outskirts. The spatially resolved BPT diagram further shows ongoing star formation in the central region for most of the blue-core galaxies. The younger central stellar population/ongoing star formation in the blue-core galaxies requires an adequate gas supply to the center. In this case, the question about "how to form the blue-core galaxies" becomes "what triggers gas inflow in those blue-core galaxies." It is well established that both the existence of a bar and interaction with companions can effectively cause gas inflow and enhance star formation in the center of a galaxy (e.g., Regan & Teuben 2004; Li et al. 2008; Lin et al. 2017; Wang et al. 2012; Holmes et al. 2015). Hydrodynamic numerical simulations suggest that interaction and merger can induce gas inflow and enhance star formation activity in the centers of galaxies (Barnes & Hernquist 1996; Borne et al. 1999). Benítez-Llambay et al. 2016 used a cosmological simulation to explore the the origin of age and metallicity gradients in dwarf spheroidal galaxies. They pointed out that the positive age gradients of dwarf spheroidal galaxies are due to merge induced gas inflow. Recently, Chen et al. (2016) and Jin et al. (2016) found that accreting counter rotating gas by a star-forming galaxy can lead to the redistribution of angular momentum through gas-gas collisions between the pre-existing and accreted gas, which largely accelerates gas inflow.

Figure 2 provides examples of galaxies with different features. From top to bottom: the first row is a kinematically misaligned galaxy; the second row is a bar galaxy; the third row is a post-merger galaxy and the fourth row is a galaxy without any obvious feature which can be relevant to gas inflows. From left to right: the left column shows the SDSS g, r, i-band images; the second column is the velocity field of stars; the third column is the velocity field of gas; the last column is D_n4000 maps. To investigate the relevant contribution of the mechanisms described above (bar, interaction and accreting counter rotating gas) to the formation of the blue-core galaxies, we summarize the properties of blue-core galaxies in Table 1. These properties include galaxy inclination and ΔPA (the PA difference between gas and stellar components). We compute the galaxy inclination angle, i, from the measured axial ratio, b/a and the r-band absolute magnitude M_r using table 8 in Padilla & Strauss (2008). We measure the difference in the kinematic PA between ionized gas and stars as $\Delta\mathrm{PA} = |\mathrm{PA}_* - \mathrm{PA}_{\mathrm{gas}}|$, where PA_* is the PA of stars and $\mathrm{PA}_{\mathrm{gas}}$ is the PA of ionized gas. The kinematic PA is measured based on established methods, defined as the counter-clockwise angle between north and a line that bisects the velocity field of gas or stars, measured on the receding side (Krajnović et al. 2006).

From Table 1, we find that $\sim$26% (28/107) of blue-core galaxies have decoupled gas-star kinematics ($\Delta\mathrm{PA} > 30°$), indicating that accreting misaligned gas might be the origin of gas inflow, and in turn the blue-cores in these galaxies. To check the morphological classification of blue-core galaxies, we reference the catalog from Galaxy Zoo 2 [2] (GZ2; Willett et al. 2013), which provides the morphological features for 304 122 galaxies from SDSS DR7 with $m_r < 17$ mag, including bars, bulges, disk shapes, spiral arms, etc. We match our galaxy sample with GZ2, finding that $\sim$ 15% (17/107) of blue-core galaxies have a bar structure, which implies that bar-induced gas inflows act as a formation mechanism of blue cores. Another $\sim$8% (9/107) manifest post-merger features, such as a tidal tail and irregular gas velocity field, indicating galaxy interaction acts as a trigger mechanism for gas inflow. For the other 53 galaxies, 15 galaxies are totally face-on, and four galaxies do not have any nebular emission, both of which make the robust measurement of ΔPA impossible. We find another 13 blue-core galaxies which are totally edge–on. In these galaxies, it is hard to identify any bar features. In summary, 49% of blue-core galaxies show obvious features, such as interaction, accreting misaligned gas and bar structure, which can lead to gas inflow. Another 26% of galaxies are totally face-on or edge-on, making it impossible for us to identify kinematical misalignment or bar

[2] `http:/zoo2.galaxyzoo.org/`

structure. For the remaining 25% of galaxies, we have not found any features that could lead to gas inflow. Thus, the formation of the blue cores in these galaxies is still a mystery.

3.2 The Gas-phase Metallicity of Blue-core Galaxies

Chemical abundance is important in constraining the evolution and SFH of galaxies. Compared with stellar metallicity which is derived from strong nebular emission, the gas-phase metallicity estimated from strong nebular emission lines includes the following advantages (Tremonti et al. 2004): (1) it can be measured in many optically faint galaxies which exhibit the highest emission-line equivalent width, since the S/N of the emission lines exceeds that of the continuum; (2) it is free from the uncertainty caused by α-enhancement and age; (3) it represents the present-day abundance rather than the average of past stellar population generations. In this section, we focus on the gas-phase metallicity of blue-core galaxies.

According to the resolved BPT diagram, most of the blue-core galaxies experience ongoing star formation in their central region. Therefore, we directly match our blue-core galaxies with the MPA/JHU catalog[1] (Tremonti et al. 2004; Brinchmann et al. 2004) to obtain the gas-phase metallicity. We procure gas-phase metallicity for 68 blue-core galaxies, 325 flat-gradient galaxies and 169 red-core galaxies.

Figure 3 shows the stellar mass–gas-phase metallicity relation. The black solid line is the median stellar mass–gas-phase metallicity relation of the SDSS DR7 star-forming galaxies, and two black dashed lines represent the $\pm 1\sigma$ error region. The blue dots are the blue-core galaxies. It is clear that most of the blue-core galaxies do not follow the median mass–metallicity relation of local star forming galaxies, and they lie above this relation by about $\sim 0.2{-}0.3$ dex, which indicates that blue-core galaxies have higher gas metallicity. This result is consistent with Chen et al. (2016) and Jin et al. (2016) who found that the blue star-forming counter-rotating galaxies with younger stellar populations in their centers (exhibiting positive D_n4000 gradients, which are common in our blue-core sample) have higher central $3''$ gas-phase metallicity than the prediction from mass-metallicity relation for local star-forming galaxies. However, the higher gas metallicity for the blue-core galaxies is still a puzzle. To compare with blue-core galaxies, we also overplot flat-gradient and red-core galaxies. The green stars are flat-gradient galaxies, while red squares are red-core galaxies. The larger symbols with $\pm 1\sigma$ error bars show the median in each mass bin. Generally speaking, there is evidence that the blue-core galaxies have higher metallicity than the flat-gradient and red-core galaxies. What is more obvious is that the median metallicity for all these three populations is higher than the median mass-metallicity relation for local star forming galaxies.

One explanation for the blue-core galaxies is due to the instantaneous enrichment from star formation. Based on the assumption of the closed-box model (Dalcanton 2007), metallicity will mainly depend on the gas mass fraction $f_{\rm gas}$ ($\equiv M_{\rm gas}/(M_{\rm gas}+M_{\rm star})$). The abundances become elevated when a large fraction of the available gas turns into stars. The low D_n4000 at the center is a hint that such stars exist. However, we keep in mind that the "external" gas likely has low metallicity and the closed-box model is a strong assumption which may not be valid for galaxies with $M_* < 10^{10.5} M_\odot$. Another disadvantage for this explanation is that it cannot explain the higher metallicity in flat-gradient and red-core galaxies.

We check the other possibilities for the high gas-phase metallicity found in blue-core, flat-gradient and red-core galaxies. The first possibility that comes to our mind is the aperture effect. Panel (a) of Figure 4 shows the redshift distribution, with the blue histogram representing blue-core galaxies. The green histogram corresponds to the redshift distribution for flat-gradient galaxies while the red histogram refers to red-core galaxies. The black histogram is for the SDSS DR7 star-forming galaxies. The vertical blue, green, red and black dashed lines mark the median of each sample. The median redshift of the MaNGA blue-core, flat-gradient and red-core galaxies with metallicity measured in the MPA/JHU catalog is $\sim$0.03, with the lowest median value for the blue-core galaxies which is much smaller than the median redshift of the DR7 star-forming galaxies sample. By combining the information expressed in these different redshift distributions with the negative gas-phase metallicity gradients in star-forming galaxies (Lian et al. 2018), we suggest that the aperture effect may partly explain the higher metallicity that is observed in the MaNGA sample. Panel (b) of Figure 4 is similar to Figure 3, and the only difference is that we add the mass-metallicity relation for a DR7 star-forming galaxy subsample with $0.01 \leq z < 0.05$ as a blue solid line, and the two blue dashed lines show the $\pm 1\sigma$ scattering region. From panel (b) of Figure 4, we find that the median stellar mass–gas-phase metallicity relation rises about 0.06 dex at $\log(M_*/M_\odot) > 9.5$ when we constrain the redshifts of SDSS DR7 star-forming galaxies to a similar range for the MaNGA sample (the blue solid line), which supports our

Table 1 The Sample of Blue-core Galaxies

MaNGAID (1)	RA (2)	Dec (3)	Redshift (4)	$\log(M_*/M_\odot)$ (5)	i (deg) (6)	ΔPA (7)	Morphology (8)
1-47705	130.996405	51.09026806	0.1263	11.57	55	168 ± 12	misaligned
1-48450	132.2615081	53.83853806	0.0304	9.45	70	6 ± 20	edge-on
1-22414	252.6189031	64.02065611	0.0923	11.19	29	105 ± 31	misaligned
1-44312	119.6379289	45.329425	0.0219	9.32	77	6 ± 22	edge-on
1-634795	263.2053689	56.90128694	0.0294	10.67	72	26 ± 4	edge-on
1-24440	264.6625581	56.82429111	0.0294	10.11	65	6 ± 4	bar
1-47248	131.8838311	53.90524194	0.0465	11.21	14	18 ± 7	face-on
1-48136	132.9127611	57.10741611	0.0256	9.97	19	167 ± 10	misaligned
1-596095	318.0865569	11.22024306	0.0175	9.96	54	12 ± 4	bar
1-121532	118.0911061	34.32654694	0.1400	11.18	60	43 ± 7	misaligned
1-90779	236.1525081	54.20930806	0.0664	11.01	24	18 ± 4	face-on
1-135239	246.4872339	41.52205194	0.0427	10.00	38	165 ± 20	misaligned
1-135227	246.704395	42.67892806	0.0304	10.01	55	6 ± 4	-
1-135512	247.7117769	40.02477111	0.0280	9.48	43	35 ± 25	misaligned
1-135506	247.9485239	39.81422306	0.0295	9.66	50	7 ± 7	disturbed gas map
1-633990	247.3041169	41.15088389	0.0296	10.49	25	6 ± 4	bar
1-135625	248.5074589	41.34795889	0.0284	10.31	39	0 ± 4	post-merger
1-135383	250.3128331	39.75236611	0.0301	10.34	75	0 ± 4	bar
1-180193	322.2420219	-0.342438889	0.0303	10.34	62	6 ± 4	-
1-178823	311.7637839	0.436801111	0.0126	9.40	51	62 ± 7	misaligned
1-179900	319.3895711	-0.134728889	0.0575	10.60	66	6 ± 4	-
1-29512	356.7518169	-0.447405	0.0712	11.13	47	6 ± 4	bar
1-37679	48.57332	-0.609693056	0.1152	11.56	41	0 ± 4	-
1-38352	51.28474389	-0.544938056	0.0376	9.94	72	12 ± 7	edge-on
1-604052	50.63658806	-0.001198889	0.0217	10.25	43	0 ± 4	-
1-36833	40.55684806	0.382961111	0.0220	9.78	80	11 ± 26	edge-on
1-37084	42.73942	0.369398056	0.0442	10.05	65	0 ± 20	bar
1-137961	139.7204331	45.72779111	0.0264	9.80	29	0 ± 11	face-on
1-138106	144.3523019	48.51546889	0.0243	9.84	53	6 ± 4	post-merger
1-137528	134.404975	41.04390306	0.0875	11.55	35	25 ± 4	-
1-138140	145.3080981	47.68859389	0.0468	10.57	31	174 ± 4	misaligned
1-155558	137.0326331	45.92095389	0.0268	9.99	66	0 ± 9	-
1-155903	141.1902419	49.44481889	0.0164	8.92	23	19 ± 122	face-on
1-145920	119.3568169	27.44038389	0.0267	9.64	54	62 ± 13	misaligned
1-605571	134.7484519	39.74883694	0.0240	9.62	79	31 ± 38	misaligned
1-217221	138.753045	42.02443611	0.0279	10.27	74	0 ± 4	face-on
1-145741	117.1774719	26.53976806	0.0155	9.16	56	19 ± 27	-
1-149211	168.9477761	50.40159806	0.0473	10.08	75	13 ± 9	edge-on
1-163516	115.7170281	22.112725	0.0286	10.72	27	6 ± 11	bar
1-167688	155.8855589	46.05774889	0.0258	9.80	18	6 ± 13	face-on
1-606105	147.6643411	44.331125	0.0154	9.48	56	0 ± 15	bar
1-167582	154.4808131	46.60324194	0.0300	9.94	64	43 ± 16	misaligned
1-197063	212.955995	52.81671694	0.0765	11.43	33	$-$	-
1-210989	246.6527239	39.85867389	0.0314	10.27	73	0 ± 4	disturbed gas map
1-211077	247.5723969	39.88943306	0.0297	10.64	55	37 ± 4	misaligned
1-209980	240.4709089	45.35196194	0.0420	10.73	44	6 ± 4	-
1-230177	124.8978181	26.36269	0.0200	9.42	61	6 ± 28	bar
1-235306	211.4226819	46.42744694	0.0674	10.94	60	0 ± 4	post-merger
1-301241	144.5264239	36.03919694	0.0225	9.84	73	18 ± 4	edge-on
1-593159	217.6299661	52.70717611	0.0448	11.06	61	6 ± 4	bar

Notes: The physical parameters describing blue-core galaxies. The first column is MaNGAID; the second and third columns are right ascension and declination, respectively; the fourth column is redshift; the fifth column is stellar mass; the sixth column is inclination angle; the seventh column is difference in the kinematic PA between star and ionized gas which is defined as $\Delta\mathrm{PA} = |\mathrm{PA}_{\mathrm{star}} - \mathrm{PA}_{\mathrm{gas}}|$; the eighth column is morphology of the galaxies. The kinematic PA is measured based on established methods (Krajnović et al. 2006).

Table 1 — *Continued.*

MaNGAID (1)	RA (2)	Dec (3)	Redshift (4)	$\log(M_*/M_\odot)$ (5)	i (deg) (6)	ΔPA (7)	Morphology (8)
1-248389	240.6580569	41.29343194	0.0348	10.59	28	0 ± 7	face-on
1-248415	241.846595	41.708925	0.0181	9.69	12	16 ± 25	face-on
1-246027	219.3966111	51.58314389	0.0437	11.00	58	–	-
1-245670	217.3248169	52.66555889	0.0305	10.51	58	0 ± 4	-
1-246517	225.9417439	49.52588	0.0192	9.42	64	56 ± 11	misaligned
1-269984	248.4627669	25.86014389	0.0512	10.80	63	7 ± 4	-
1-316872	235.1526381	28.51245611	0.0328	10.80	38	6 ± 4	-
1-375134	232.5510569	27.13410694	0.0326	10.69	66	18 ± 4	bar
1-604860	118.18416	45.94927889	0.0517	11.26	22	7 ± 4	face-on
1-339300	118.6555369	46.98821889	0.0172	9.29	58	29 ± 24	-
1-339010	115.9640169	44.72431889	0.0313	10.34	78	0 ± 4	edge-on
1-378753	119.9882839	50.42771611	0.0226	9.27	79	19 ± 18	edge-on
1-379199	119.7796381	52.74717306	0.0192	8.96	49	24 ± 90	-
1-379261	118.80521	52.84707694	0.0233	9.26	53	24 ± 56	-
1-386452	136.2283319	28.38430389	0.0269	10.62	73	6 ± 4	edge-on
1-386695	137.9834931	27.89928889	0.0474	10.11	72	40 ± 4	misaligned
1-386263	136.2400531	27.72762806	0.0214	8.85	71	180 ± 114	misaligned
1-419380	183.00791	35.40440889	0.0235	9.89	59	174 ± 4	misaligned
1-456405	193.6030969	27.36395111	0.0261	9.82	51	50 ± 10	misaligned
1-456772	194.0254211	27.67810194	0.0165	9.12	56	12 ± 11	-
1-457009	196.0468689	27.49043806	0.0178	9.93	31	37 ± 4	misaligned
1-456355	194.2998231	27.10333611	0.0245	9.64	68	13 ± 31	-
1-486227	165.9619489	23.00648611	0.0355	9.43	21	12 ± 122	face-on
1-489877	171.3342369	22.732725	0.0238	9.26	58	6 ± 18	-
1-487046	165.8928239	21.04946389	0.0210	9.08	75	174 ± 45	misaligned
1-92547	243.1025511	48.52988806	0.0578	10.87	66	6 ± 4	bar
1-95657	253.6327681	37.63140694	0.0628	10.96	25	18 ± 13	face-on
1-134004	238.4486061	47.40498194	0.0186	9.38	58	143 ± 10	misaligned
1-133941	239.0306389	48.03087889	0.0189	9.44	45	6 ± 4	bar
1-133922	239.1956469	47.99551306	0.0175	9.80	78	18 ± 7	edge-on
1-147507	152.7732731	46.89951389	0.0251	9.39	63	0 ± 9	-
1-147815	153.36552	47.51622	0.0253	9.90	66	149 ± 9	misaligned
1-217500	146.2734339	45.58703806	0.0162	9.38	77	174 ± 28	misaligned
1-38012	50.14511194	-1.095875	0.0214	9.12	26	0 ± 41	face-on
1-109378	51.16989111	-0.681481111	0.0391	10.84	54	0 ± 4	-
1-202097	56.92716	0.030438889	0.0405	9.87	80	0 ± 10	edge-on
1-38168	49.92932889	0.565456111	0.0243	10.06	73	26 ± 7	bar
1-38166	49.94683889	0.623805	0.0247	9.28	14	–	face-on
1-298715	125.3616739	24.45308111	0.0198	10.12	45	19 ± 7	disturbed gas map
1-298727	125.8531731	24.67344306	0.0156	8.94	70	43 ± 75	misaligned
1-274368	155.6929019	37.67356611	0.0226	9.24	52	19 ± 25	bar
1-255928	163.9934511	44.38083389	0.0373	9.37	58	93 ± 13	misaligned
1-277246	166.1877919	45.15646194	0.0220	9.37	19	136 ± 19	misaligned
1-284526	198.18911	46.93497889	0.0277	10.46	43	0 ± 4	-
1-258599	186.1809689	44.41078611	0.1256	11.38	67	23 ± 4	disturbed gas map
1-252046	217.5479881	39.90518694	0.0257	9.57	69	12 ± 11	-
1-251788	215.2292189	40.12103111	0.0175	9.97	33	7 ± 13	-
1-256203	166.1973969	44.02182889	0.0256	10.14	54	56 ± 4	misaligned
1-258306	183.5789719	43.53527389	0.0241	9.54	72	6 ± 9	edge-on
1-321963	227.0696119	42.91640611	0.0183	8.81	13	–	face-on
1-269632	247.56098	26.20647889	0.1315	11.38	21	0 ± 4	bar
1-322787	235.9205011	39.54035	0.0635	10.60	26	6 ± 21	post-merger
1-322113	229.3089061	44.01803889	0.1223	11.40	26	6 ± 4	face-on
1-173958	167.3060131	49.519445	0.0724	11.03	59	6 ± 11	bar
1-277328	164.44615	44.65466194	0.0374	9.57	57	87 ± 31	misaligned
1-279532	170.8082831	46.99777194	0.0248	10.26	66	180 ± 4	vs
1-631278	221.438	51.5808	0.0296	11.03	36	30 ± 4	merger

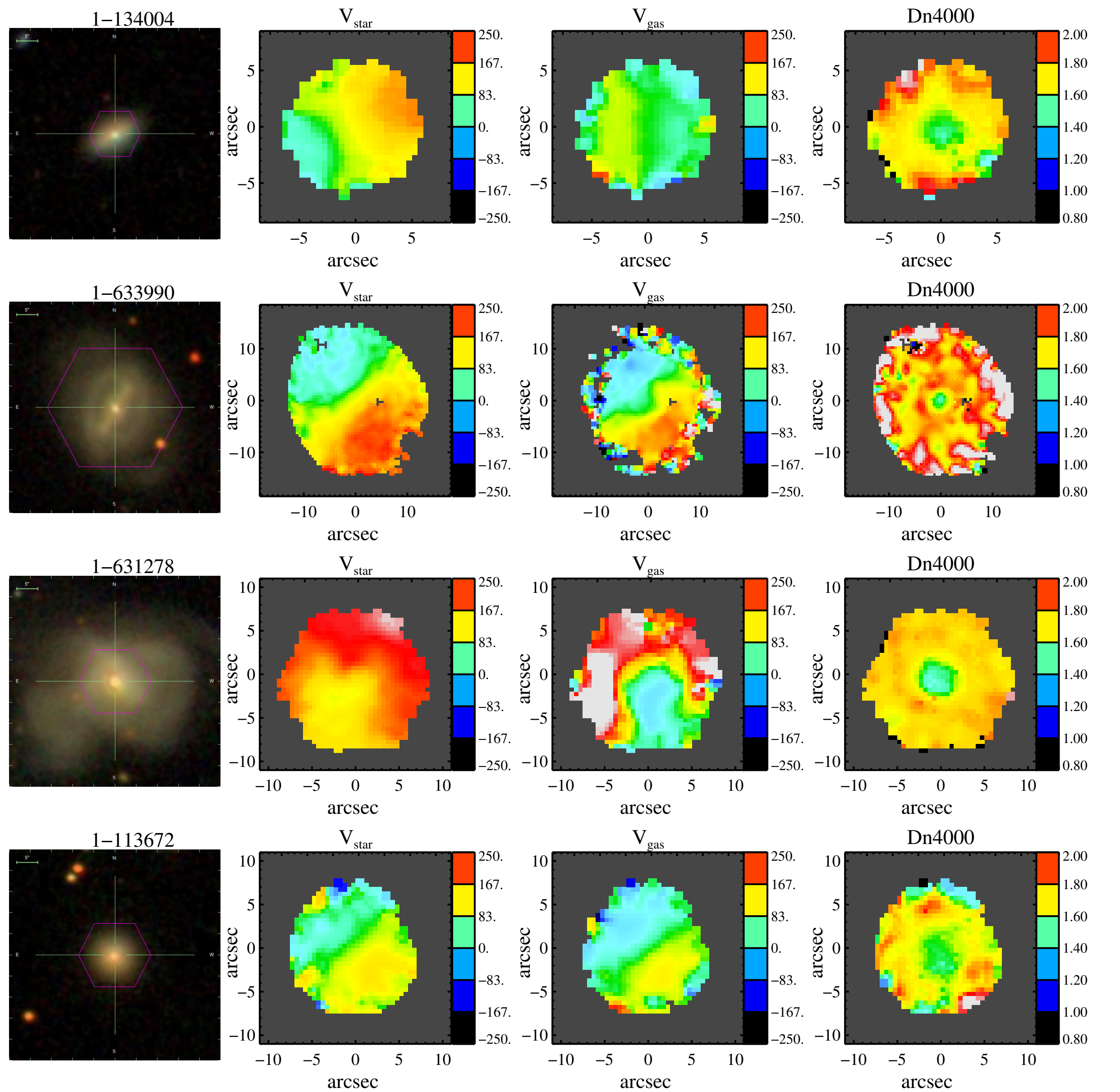

Fig. 2 Examples of galaxies with different features. The first row is a kinematically misaligned galaxy, the second row is a bar galaxy, the third row is a post-merger galaxy and the fourth row is a galaxy without any obvious feature. The left column shows the SDSS g, r, i-band images, the second column displays the velocity field of stars, the third column depicts the velocity field of gas and the last column exhibits D_n4000 maps.

expectation that the aperture effect partly influences the observed mass–metallicity relation.

We also explore the hardness of the radiation field for the blue-core, flat-gradient and red-core galaxies with metallicity measurements from the MPA/JHU catalog. Trouille et al. (2011) used [Ne III]/[O II] vs. $(g-z)^{0.0}$ color to separate star-forming galaxies from AGN for galaxies with $z < 1.4$. They refer to this new diagnostic as the Trouille, Barger and Tremonti (TBT) diagram. The principle of the TBT diagram is that: (1) the ratio of [Ne III]/[O II] can effectively separate metal-rich star-forming galaxies from AGN since [Ne III] emission indicates the presence of highly ionized gas and is much stronger than [O II] in high-excitation AGN; (2) although metal-poor star-forming galaxies have high values of [Ne III]/[O II] as a result of less line blanketing which enables a harder stellar radiation field, fortunately, metal-poor galaxies also tend to be bluer, so their $(g-z)^{0.0}$ color can be used to distinguish them from AGN (which tend to be bulge dominated and redder).

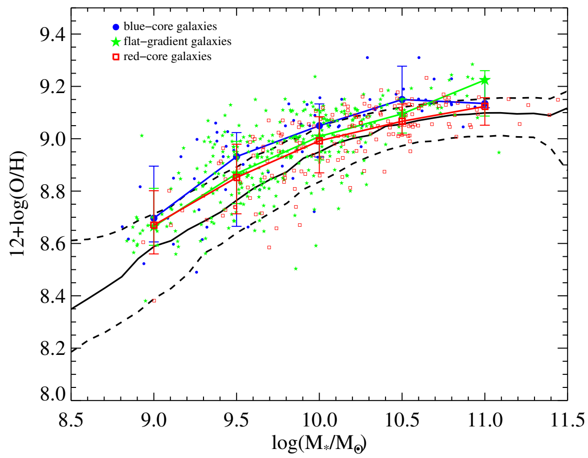

Fig. 3 Stellar mass–gas phase metallicity relation. The *black solid line* represents the median stellar mass-metallicity relation of the SDSS DR7 star-forming galaxies, and two *black dashed lines* indicate the $\pm1\sigma$ error region. The *blue dots* are the blue-core galaxies. The *green stars* are flat-gradient galaxies. The *red squares* are red-core galaxies. The larger symbols indicate the median in each mass bin. Error bars represent the 16th and 84th percentiles in each mass bin.

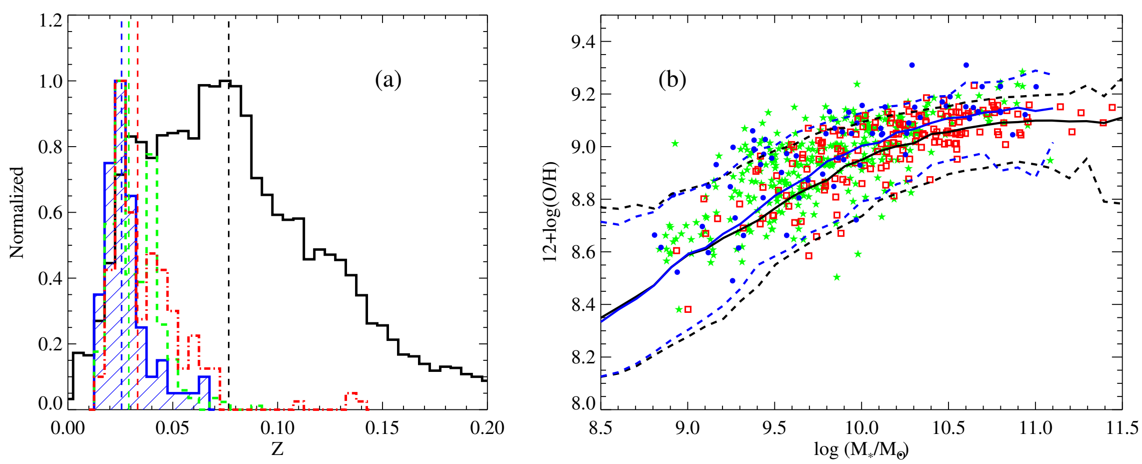

Fig. 4 Panel (a) shows the distribution of redshifts. The *blue histogram* is for blue-core galaxies. The *green histogram* is for flat-gradient galaxies. The *red histogram* is for red-core galaxies. The *black histogram* is for SDSS DR7 star-forming galaxies. The *vertical blue*, *green*, *red* and *black dashed lines* indicate the medians of redshift for each sample. Panel (b) is the relation between stellar mass and gas-phase metallicity. The *black solid line* represents the median stellar mass-metallicity relation for the SDSS DR7 star-forming galaxies, and two *black dashed lines* indicate the $\pm1\sigma$ scattering region. The *blue solid line* signifies the median stellar mass-metallicity relation of the SDSS DR7 star-forming galaxies with $0.01 < z < 0.05$, and the two *blue dashed lines* indicate the $\pm1\sigma$ scattering region. The *blue dots* are the blue-core galaxies. The *green stars* are flat-gradient galaxies. The *red squares* are red-core galaxies.

In the left panel of Figure 5, we overplot our blue core galaxies on the TBT diagram as well as flat-gradient and red-core galaxies. The cyan, green and red contours represent the SDSS DR7 star-forming galaxies, composites and AGN classified by the BPT diagram, respectively. The black dashed line separates the star-forming galaxies from AGN according to the TBT diagram. From the left panel of Figure 5, we find that on one hand, these blue-core, flat-gradient and red-core galaxies have a wide coverage in the radiation field hardness, thus the hardness of the radiation field is not a primary driver of their high metallicity; while on the other hand, they have redder $(g-z)^{0.0}$ color (larger than 0.5) by comparing with the local star-forming sample. We also test whether the metallicity depends on $(g-z)^{0.0}$ color. The right panel of Figure 5 shows the stellar mass–metallicity relation. The cyan line represents the median stellar mass-metallicity relation for the SDSS DR7 star-forming galaxies with $(g-z)^{0.0} > 0.5$ while the magenta line represents the relation for galaxies with

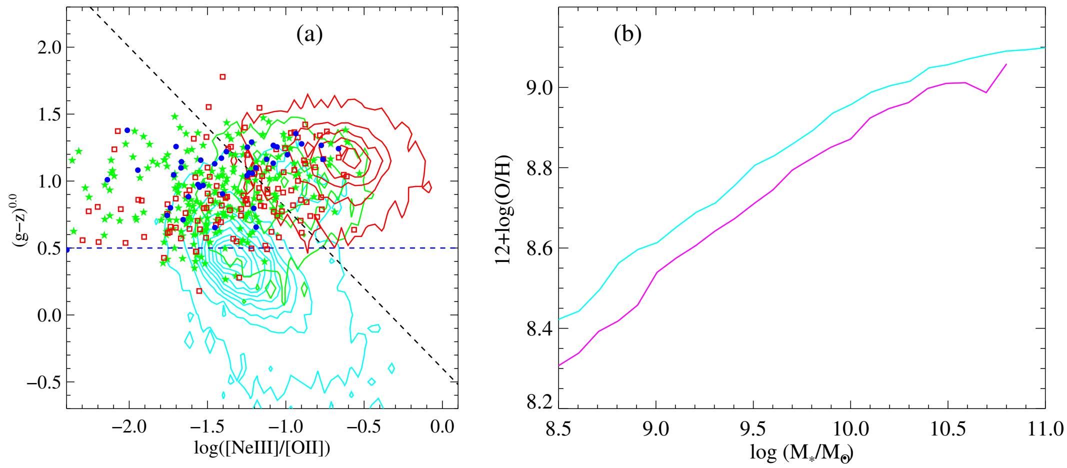

Fig. 5 Panel (a) shows the TBT diagram (Trouille et al. 2011). The *cyan contours* indicate the star-forming (DR7) galaxies classified by the BPT diagram, *green contours* signify composites galaxies and *red contours* correspond to AGN. The *blue dashed line* marks the position with $(g-z)^{0.0} = 0.5$. The *black dashed line* indicates the separation of TBT-SF and TBT-AGN from Trouille et al. (2011). Panel (b) shows the relation between stellar mass and gas-phase metallicity. The *cyan line* represents the median stellar mass-metallicity relation of the SDSS DR7 star-forming galaxies with $(g-z)^{0.0} > 0.5$ while the *magenta line* indicates the relation for galaxies with $(g-z)^{0.0} < 0.5$.

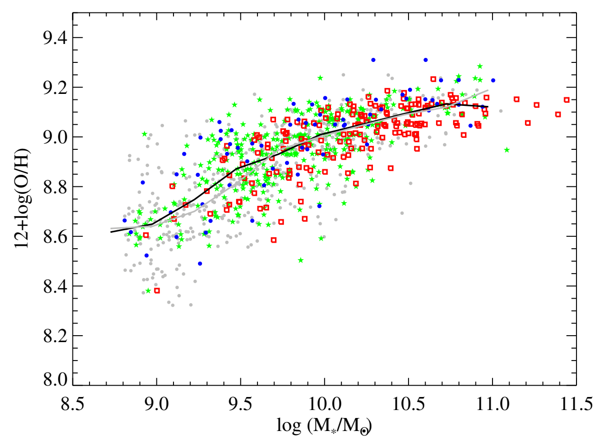

Fig. 6 The stellar mass vs. gas phase metallicity for the MaNGA sample and control sample. The *blue dots* represent the blue-core galaxies. The *green stars* signify flat-gradient galaxies. The *red squares* indicate red-core galaxies. The *grey dots* mark the control sample. The *black solid line* is the median for our sample while *grey solid line* is median for the control sample.

$(g-z)^{0.0} < 0.5$. From the right panel of Figure 5, we find that galaxies with redder color have higher gas metallicity.

To quantify the contribution of aperture effect and galaxy color to the observed mass–metallicity relation, we select a control sample for the blue-core, flat-gradient and red-core galaxies from the SDSS DR7 star-forming sample. The control sample is closely matched in redshift and $(g-r)^{0.0}$ color with $|\Delta z| < 0.001$ and $|\Delta z| < 0.001$.

Figure 6 shows the stellar mass vs. gas-phase metallicity for our sample and the control sample. The blue dots represent the blue-core galaxies. The green stars signify flat-gradient galaxies. The red squares indicate red-core galaxies. The grey dots mark the control sample. The black solid line is the median of our sample while grey solid line is median for the control sample. We find that the median stellar mass-metallicity relation has no significant difference for our sample and the control sample, suggesting that higher central metallicity observed in MaNGA galaxies can be explained as a result of redder color and lower redshift.

4 SUMMARY

We select 107 blue-core galaxies from MaNGA MPL5, studying their morphology, kinematics as well as gas phase metallicity. The main conclusions include the following:

(1) The formation of blue-core galaxies corresponds to gas inflow. In our sample, 26% of blue-core galaxies have decoupled gas-star kinematics, indicating external gas accretion; 15% have bar-like structure and 8% show post-merger features, such as tidal tails and an irregular gas/star velocity field. All these processes/features, such as accreting external misaligned gas, interaction and bar, can trigger gas inflow. Another 26% of galaxies are totally face-on/edge-on, making the identification of kinematical misalignment and bar features impossible.

(2) By comparing with the SDSS DR7 star-forming galaxy sample, we find that the blue-core galaxies have higher central gas phase metallicity than the prediction by the local mass-metallicity relation, which is consistent with the results of Chen et al. (2016), Jin et al. (2016) and Wake et al. (2017). We explore the origin of the higher metallicity, finding that not only the blue-core galaxies but also the flat-gradient and red-core galaxies all have higher metallicity. This can be explained as a combined effect of redshift and galaxy color. On one hand, the MaNGA sample has a lower redshift distribution than the SDSS DR7 sample. Considering the negative metallicity gradient in the local star-forming galaxies, we can easily understand the higher central metallicity in MaNGA galaxies. On the other hand, the mass-metallicity relation also depends on galaxy colors at the same stellar mass, and galaxies with redder colors have higher gas-phase metallicity. The larger $(g-z)^{0.0}$ colors of the MaNGA galaxies selected in our sample can partly explain the higher metallicity that we observe.

Acknowledgements We are very grateful to the anonymous referee for comments and suggestions that improved the manuscript. This work was supported by the National Key R&D Program of China (2018YFA0404502 and 2017YFA0402704), the National Natural Science Foundation of China (Grant Nos. 11733002 and 11773013) and the Excellent Youth Foundation of the Jiangsu Scientific Committee (BK 20150014). Y.C. acknowledges support from the National Natural Science Foundation of China (Grant No. 11573013). Funding for the Sloan Digital Sky Survey IV has been provided by the Alfred P. Sloan Foundation, the U.S. Department of Energy Office of Science and the Participating Institutions. SDSS-IV acknowledges support and resources from the Center for High-Performance Computing at the University of Utah. The SDSS web site is `www.sdss.org`.

SDSS-IV is managed by the Astrophysical Research Consortium for the Participating Institutions of the SDSS Collaboration including the Brazilian Participation Group, the Carnegie Institution for Science, Carnegie Mellon University, the Chilean Participation Group, the French Participation Group, Harvard-Smithsonian Center for Astrophysics, Instituto de Astrofísica de Canarias, The Johns Hopkins University, Kavli Institute for the Physics and Mathematics of the Universe (IPMU)/University of Tokyo, Lawrence Berkeley National Laboratory, Leibniz Institut für Astrophysik Potsdam (AIP), Max-Planck-Institut für Astronomie (MPIA Heidelberg), Max-Planck-Institut für Astrophysik (MPA Garching), Max-Planck-Institut für Extraterrestrische Physik (MPE), National Astronomical Observatories of China, New Mexico State University, New York University, University of Notre Dame, Observatário Nacional/MCTI, The Ohio State University, Pennsylvania State University, Shanghai Astronomical Observatory, United Kingdom Participation Group, Universidad Nacional Autónoma de México, University of Arizona, University of Colorado Boulder, University of Oxford, University of Portsmouth, University of Utah, University of Virginia, University of Washington, University of Wisconsin, Vanderbilt University and Yale University.

References

Abazajian, K. N., Adelman-McCarthy, J. K., Agüeros, M. A., et al. 2009, ApJS, 182, 543
Baldwin, J. A., Phillips, M. M., & Terlevich, R. 1981, PASP, 93, 5
Barnes, J. E., & Hernquist, L. 1996, ApJ, 471, 115
Benítez-Llambay, A., Navarro, J. F., Abadi, M. G., et al. 2016, MNRAS, 456, 1185
Blanton, M. R., Kazin, E., Muna, D., Weaver, B. A., & Price-Whelan, A. 2011, AJ, 142, 31
Borne, K. D., Bushouse, H., Colina, L., et al. 1999, Ap&SS, 266, 137
Brinchmann, J., Charlot, S., White, S. D. M., et al. 2004, MNRAS, 351, 1151
Bundy, K., Bershady, M. A., Law, D. R., et al. 2015, ApJ, 798, 7
Chen, Y.-M., Shi, Y., Tremonti, C. A., et al. 2016, Nature Communications, 7, 13269
Dalcanton, J. J. 2007, ApJ, 658, 941
Drory, N., MacDonald, N., Bershady, M. A., et al. 2015, AJ, 149, 77
Gallart, C., Stetson, P. B., Meschin, I. P., Pont, F., & Hardy, E. 2008, ApJ, 682, L89
Gunn, J. E., Siegmund, W. A., Mannery, E. J., et al. 2006, AJ, 131, 2332

Holmes, L., Spekkens, K., Sánchez, S. F., et al. 2015, MNRAS, 451, 4397
Jin, Y., Chen, Y., Shi, Y., et al. 2016, MNRAS, 463, 913
Kauffmann, G., Heckman, T. M., Tremonti, C., et al. 2003, MNRAS, 346, 1055
Kewley, L. J., Dopita, M. A., Sutherland, R. S., Heisler, C. A., & Trevena, J. 2001, ApJ, 556, 121
Krajnović, D., Cappellari, M., de Zeeuw, P. T., & Copin, Y. 2006, MNRAS, 366, 787
Law, D. R., Yan, R., Bershady, M. A., et al. 2015, AJ, 150, 19
Law, D. R., Cherinka, B., Yan, R., et al. 2016, AJ, 152, 83
Li, C., Kauffmann, G., Heckman, T. M., White, S. D. M., & Jing, Y. P. 2008, MNRAS, 385, 1915
Li, C., Wang, E., Lin, L., et al. 2015, ApJ, 804, 125
Lian, J., Thomas, D., Maraston, C., et al. 2018, MNRAS, 476, 3883
Lin, L., Li, C., He, Y., Xiao, T., & Wang, E. 2017, ApJ, 838, 105
Lin, L., Zou, H., Kong, X., et al. 2013, ApJ, 769, 127
Padilla, N. D., & Strauss, M. A. 2008, MNRAS, 388, 1321
Pan, Z., Li, J., Lin, W., et al. 2015, ApJ, 804, L42
Pérez, E., Cid Fernandes, R., González Delgado, R. M., et al. 2013, ApJ, 764, L1
Regan, M. W., & Teuben, P. J. 2004, ApJ, 600, 595
Smee, S. A., Gunn, J. E., Uomoto, A., et al. 2013, AJ, 146, 32
Strauss, M. A., Weinberg, D. H., Lupton, R. H., et al. 2002, AJ, 124, 1810
Tremonti, C. A., Heckman, T. M., Kauffmann, G., et al. 2004, ApJ, 613, 898
Trouille, L., Barger, A. J., & Tremonti, C. 2011, ApJ, 742, 46
Wake, D. A., Bundy, K., Diamond-Stanic, A. M., et al. 2017, AJ, 154, 86
Wang, J., Kauffmann, G., Overzier, R., et al. 2011, MNRAS, 412, 1081
Wang, J., Kauffmann, G., Overzier, R., et al. 2012, MNRAS, 423, 3486
Wang, E., Li, C., Xiao, T., et al. 2018, ApJ, 856, 137
Willett, K. W., Lintott, C. J., Bamford, S. P., et al. 2013, MNRAS, 435, 2835
Yan, R., Tremonti, C., Bershady, M. A., et al. 2016, AJ, 151, 8